Biomass and Bioenergy 168 (2023) 106656

Contents lists available at ScienceDirect

Biomass and Bioenergy

journal homepage: www.elsevier.com/locate/biombioe

CFD modelling of spatiotemporal evolution of detailed tar species in a downdraft gasifier

Ahmed M. Salem [a,b,*], Manosh C. Paul [a,**]

[a] Systems, Power & Energy Research Division, James Watt School of Engineering, University of Glasgow, Glasgow, G12 8QQ, UK
[b] Mechanical Power Department, Faculty of Engineering, Tanta University, Tanta, Egypt

ARTICLE INFO

Keywords:
Bioenergy
Gasification
Tar kinetics
Downdraft gasifier
CFD

ABSTRACT

The rising demand for renewable energy around the world has sparked interest in biomass gasification. However, the technology greatly suffers because of tar species produced during the gasification process, which limits direct use of the produced gas. To address this issue, the paper presents a novel piece of work that focuses on the formation and evolution of tar species consisting of benzene, naphthalene, toluene, and phenol. A two-dimensional numerical model for a downdraft biomass gasifier is developed with a total of 20 thermochemical kinetic reactions to investigate the formation of tar species in the gasifier with the effect of residence time. The model's predictions are validated with the experimental and kinetic data and found to be in good agreement. Besides, the model's ability to simulate the producer gas production from a downdraft gasifier is examined. Reaction rates for volatiles decomposition, combustion, and gasification reactions under different working conditions are investigated. Overall, benzene has the highest concentration of the selected tar species, followed by naphthalene, and with relatively modest amounts of phenol and toluene.

1. Introduction

The increase trend of the world's population, along with rising energy demand and continuous depletion of fossil fuels, encourages the development of renewable energy technologies. Biomass, as a renewable energy source, is considered to be clean, sustainable, and does not contribute to the generation of greenhouse gases. Besides, biomass can be converted to energy through different techniques including pyrolysis, gasification, and combustion [1,2], and [3].

Biomass gasification, as the topic of this paper, is a promising approach for producing syngas and power [4]. However, a gasifier's design and operation involve a complex process that requires an intensive time-consuming experiment to study the technology and obtain the optimum working parameters. On the other hand, modelling is a complementary technique that can be used to design and control the process of gasification using a wide set of validation and test data [5], and [6].

To date, different equilibrium ([7]), and kinetic models ([8–10], and [11]) have been used to model biomass gasification. However, these models have certain limitations when it comes to analysing the gasification process since the interaction between solid and gas phases reactions during the gasification process requires an in-depth understanding, which cannot be achieved with an equilibrium/kinetic modelling. Gasifier design also has a strong effect on the syngas composition and quality. These limitations were overcome using a Computational Fluid Dynamics (CFD) model, which involves a combined solution of the transports of mass, momentum, energy, turbulence, and hydrodynamics [12]. Different CFD models ([6,13,14]) were presented to simulate the process of gasification in biomass gasifiers with various gasifier types and feedstocks. Babu and Sheth [11] developed a 1D steady-state model using a finite difference method to predict the gas composition and temperature along the reduction zone of a downdraft gasifier. They used four main gasification reactions in their model besides a correlation to describe velocity, pressure, and temperature distribution along the reduction zone. Their results were compared to experimental data and found to be in good agreement.

Fletcher et al. [15] employed a Lagrangian approach to the biomass gasification process in an entrained flow gasifier. Transport equations consisting of a set of heterogeneous reactions were solved to determine the concentration of different gas species. The model was able to predict the temperature and syngas composition at the gasifier outlet under various working conditions. While Yu et al. [16] presented a numerical simulation model for a bubbling fluidized bed coal gasifier using the kinetic theory of granular flow. The model was used to study the

* Corresponding author. Systems, Power & Energy Research Division, James Watt School of Engineering, University of Glasgow, Glasgow, G12 8QQ, UK.
** Corresponding author.
E-mail addresses: Ahmed_salem@f-eng.tanta.edu.eg (A.M. Salem), Manosh.Paul@glasgow.ac.uk (M.C. Paul).

https://doi.org/10.1016/j.biombioe.2022.106656
Received 10 April 2022; Received in revised form 28 September 2022; Accepted 13 November 2022
Available online 25 November 2022

Nomenclature

Upper case letters

A	Pre-exponential factor (units vary)
D	Diameter (m)
$D_{i,m}$	Mass diffusion coefficient for species i in the mixture
$D_{T,i}$	Thermal diffusion coefficient for species i
D_t	Turbulent diffusivity
E	Energy (kJ/mol)
F_i	External body forces (N)
G_b	Turbulence kinetic energy due to buoyancy
G_k	Turbulence kinetic energy due to the mean velocity gradients
H	Enthalpy (kJ/mol)
I	Unit tensor
J_i	Diffusion flux of species i
K	Kinetic constant (s^{-1})
M	Molecular mass (kg/mol)
P	Pressure (Pa)
R	Net rate of formation (mol $m^{-3}s^{-1}$)
Re	Reynolds number
R_i	Net rate of production of species i by chemical reaction
S_i	Mass added to the continuous phase from the dispersed phase
S_k	Source terms for the kinetic energy
S_ε	Source terms for rate of dissipation
Sc_t	Schmidt number for turbulent flow
T	Temperature (K)
T_R	Temperature of radiation (K)
V	Volume (m^3)
Y_i	Mass fraction of species i
Y_M	Contribution of the fluctuating dilatation in compressible turbulence to the overall dissipation rate

Lower case letters

g_i	Gravitational acceleration
h	Convective heat transfer coefficient ($W/m^2.K$)
h_{fg}	Latent heat (J/kg)
m_p	Mass of particle (kg)
x_i	Number of mole species

*Greek **letters***

ρ	Density
$\sum$	Summation
Δ	Change in state
$\tau_{i,j}$	Stress tensor
μ	Molecular viscosity
σ_k	Turbulent Prandtl numbers for k
σ_ε	Turbulent Prandtl numbers for ε
μ_t	Turbulent viscosity
ρ_p	Density of particle
ε_p	Particle emissivity
σ	Stefan Boltzmann constant, $\left(5.67 \times 10^{-8} \frac{kg}{s^{-3}K^{-4}}\right)$

List of Acronyms

VOF	Volume of fluid
MC	Moisture content (%)
A/F	Air to fuel ratio
ER	Air equivalence ratio
HHV	Higher heating value (MJ/Nm^3)
Nm^3	Normal cubic meter
CFD	Computational Fluid Dynamics
DPM	Discrete phase model
PRESTO	PREssure STaggering Option
RANS	Reynolds Averaged Navier-Stokes

relationship between the gasifier height and gas composition, temperature, and velocity along the gasifier bed.

With regard to the CFD modelling of a downdraft gasifier, Gupta et al. [17] presented a 2D model of a 10 kW downdraft biomass gasifier using ANSYS software. Wu et al. [18] also developed a 2D Euler-Euler CFD model for simulating the gas and solid phase interactions in a downdraft biomass gasifier with highly preheated air and steam. While Murugan and Sekhar [19] conducted a 2D numerical simulation of an Imbert biomass gasifier to study selected biomass feedstocks (e.g., coconut shell, cow dung, rice husk, rubber seed kernel shell, and rubber wood) which were available at a remote area. The study showed the effect of changing the equivalence ratio (ER) on the producer gas quality, composition, and heating value. The results demonstrated that ER within the range of 0.24–0.26 resulted in the optimum performance of the gasifier and particularly, the rubber seed kernel shell was the most suitable feedstock for producing syngas with a higher heating value.

Most recently, Kumar and Paul [6] presented a 2D model of a 20-kW downdraft gasifier in which a Eulerian-Lagrangian approach was used, and the model included the four main zones of gasifier such as drying, pyrolysis, oxidation, and reduction. They provided a set of chemical reaction data, and the model was validated against experimental and kinetic results from literature. A detailed result of the gas species formation along the gasifier as well as temperature profile was also presented under different ERs, however, they only showed the results for ER $>$ 0.35, which appears to be slightly high in the context of gasification. The model was later extended to 3D [13] to investigate the rubber wood gasification inside the entire reactor. Again, the Eulerian-Lagrangian approach with the discrete phase model was used to account the solid/gas phase interactions.

Experimental studies have particularly focused on investigating the nature of the formation and destruction of tar compounds because tar limits the use of producer gas. However, experimental studies regarding tar formation and destruction are a costly and time-consuming process. On the other hand, tar involves complex compounds and could form in hundreds of different chemical compounds [20]. Equilibrium and kinetic models were built to simulate gasifier operation including tar formation e.g. see Refs. [20–22], and [23]. Kinetic models depend on a detailed chemical reaction that does not depend on reactor geometry. These limitations in kinetic models are addressed through a Computational Fluid Dynamics (CFD) model, which involves a combined solution of the transports of mass, momentum, energy, turbulence and hydrodynamics of flow. It can give a better understanding of the interactions between different phases and reactions inside the gasifier. The results can then be used to optimise the work of downdraft gasifiers that lead to the production of higher value syngas.

According to the literature review provided above, none of the CFD modelling work to-date has reported the formation and distribution of tar species within a downdraft gasifier in both steady and unsteady states. The current research work presents a 2D CFD modelling of an air-blown downdraft gasifier, and it addresses a major knowledge gap in the literature on the fundamental understanding of the evolution and formation of detailed tar species such as benzene, naphthalene, toluene and phenol. The selected tar species are always found in large amounts of approximately 70–95% ([23–25]) besides they represent primary (phenol), secondary (toluene), and tertiary (benzene, and naphthalene) tars. The concentration of remaining tar species (such as xylene, indene, pyrene, cresol and xylenol) can be ignored because of their small amount or a lack of chemical data and kinetic rate reactions that can help

develop a stable kinetic code ([21], and [26]).

To the best of our knowledge, the selected tar species to be modelled in gasifier has not been computationally investigated in earlier works. Both the steady and unsteady CFD approaches will help further to clarify the tar formation and destruction throughout the gasification process, resulting in a high purity syngas product.

2. Model description

A 20-kW downdraft biomass gasifier's model is developed based on the design presented earlier in the kinetic modelling work of the authors [5]. The gasifier design is composed of the four main zones: drying, pyrolysis, oxidation, and gasification/reduction. The gasification process is governed by a set of integrated kinetics, which begin with drying, followed by volatile break-up in the pyrolysis zone, then oxidation and reduction. A total of 20 thermochemical kinetic rate reactions are implemented in the ANSYS version 19.0 software to accommodate the volatiles break-up and other reactions involved in the process.

A schematic diagram of the gasifier model is shown in Fig. 1. The gasifier uses air as a gasifying agent to be fed through the air inlets placed around the combustion zone. Biomass is fed from the top of the gasifier, while any residual ash and char to be collected from the bottom where the model assumes that all the char to be fully consumed within the reduction zone. Producer gas is discharged through the outlet pipes fitted at the bottom of the gasifier. The gasifier is an Imbert type downdraft gasifier with a throat ratio (throat to gasifier diameter) of 0.284 (Fig. 1). Throat diameter is 6.2 cm, where air is injected through the air-inlet nozzle having the diameter of D = 18 cm located at the combustion zone of the gasifier. The full design of the gasifier is verified numerically and experimentally through the kinetic model of the current authors [5].

2.1. Governing equations

The governing equations include the conservation of energy, mass, momentum, and species transport which are built-in in the ANSYS [27] as presented below:

Energy conservation:

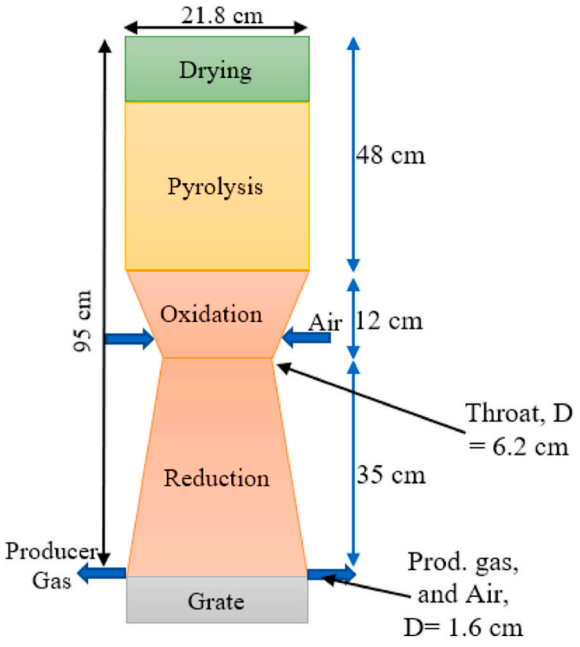

Fig. 1. Gasifier schematic showing the design and various zones.

$$\frac{\partial}{\partial t}(\rho E)+\nabla.\left(\vec{v}(\rho E+p)\right)=-\nabla.\left[\sum_j h_j J_j\right]+S_h \tag{1}$$

Mass conservation:

$$\frac{\partial \rho}{\partial t}+\frac{\partial(\rho u_i)}{\partial x_i}=S_i \tag{2}$$

Momentum conservation:

$$\frac{\partial(\rho u_i)}{\partial t}+\frac{\partial\left(\rho u_i u_j\right)}{\partial x_j}=-\frac{\partial p}{\partial x_i}+\frac{\partial \tau_{ij}}{\partial x_j}+\rho g_i+F_i \tag{3}$$

where the stress tensor τ_{ij} is defined as

$$\tau_{ij}=\mu\left[\left(\frac{\partial u_i}{\partial x_j}+\frac{\partial u_j}{\partial x_i}\right)-\frac{2}{3}\nabla.u_{ij}I\right] \tag{4}$$

and S_i is the mass added to the continuous phase from the dispersed second phase, ρg_i is the gravitational body forces, F_i is the external body forces, I is the unit tensor, E is energy, and h is enthalpy.

The Reynolds Averaged Navier-Stokes (RANS) [27] equations are derived by time averaging of equations (2)–(4). The Reynolds stresses employed in the equations are modelled through the Boussinesq hypothesis that depends on turbulence model. Turbulence kinetic energy, k, and its dissipation rate, ε, are calculated through the following equations, representing the standard k- ε viscosity model.

$$\frac{\partial}{\partial x_i}(\rho k u_i)=\frac{\partial}{\partial x_j}\left[\left(\mu+\frac{\mu_t}{\sigma_k}\right)\frac{\partial k}{\partial x_j}\right]+G_k+G_b-\rho\varepsilon-Y_M+S_k \tag{5}$$

$$\frac{\partial}{\partial x_i}(\rho \varepsilon u_i)=\frac{\partial}{\partial x_j}\left[\left(\mu+\frac{\mu_t}{\sigma_\varepsilon}\right)\frac{\partial \varepsilon}{\partial x_j}\right]+C_{1\varepsilon}\frac{\varepsilon}{k}(G_k+C_{3\varepsilon}G_b)-C_{2\varepsilon}\rho\frac{\varepsilon^2}{k}+S_\varepsilon \tag{6}$$

where σ_k and σ_ε are the turbulent Prandtl numbers for k, and ε respectively, G_b is the turbulence kinetic energy due to buoyancy, G_k is the turbulence kinetic energy due to mean velocity gradients, Y_M is the contribution of the fluctuating dilatation in compressible turbulence to the overall dissipation rate, S_k, and S_ε are the source terms for the kinetic energy, and the rate of dissipation respectively. The values of constants used are $C_{1\varepsilon}=1.44$; $C_{2\varepsilon}=1.92$; $\sigma_k=1.0$; $\sigma_\varepsilon=1.3$ [22].

The species transport equation [27] is described as

$$\frac{\partial}{\partial t}(\rho Y_i)+\nabla.(\rho\vec{u}Y_i)=-\nabla.\vec{J}_i+R_i+S_i \tag{7}$$

where Y_i is the mass fraction of species, R_i is the net rate of production of species i by chemical reaction, S_i is the rate addition by the dispersed phase plus any UDF source, and J_i is the diffusion flux of species i. While the diffusion flux for turbulent flow is represented by

$$\vec{J_i}=-\left(\rho D_{i,m}+\frac{\mu_t}{Sc_t}\right)\nabla Y_i-D_{T,i}\frac{\nabla T}{T} \tag{8}$$

$$Sc_t=\frac{\mu_t}{\rho D_t} \tag{9}$$

where $D_{i,m}$ is the mass diffusion coefficient for species i in the mixture, $D_{T,i}$ is the thermal diffusion coefficient for species i in the mixture, D_t is the turbulent diffusivity, and Sc_t is the Schmidt number for turbulent flow.

Biomass particles are modelled by discrete phase model (DPM) [27] – a Lagrangian approach. The model considers particles trajectory by a continuous phase of fluid. The interaction between particles is taken into account considering the heat and mass transfer as the main term in the governing equations. Particle trajectory is written and calculated by integrating the force balance on a particle where this balance equates the particle inertia force with the other forces acting on the particle as described in equations 10–14.

Force balance:

$$\frac{\partial \overrightarrow{u_p}}{\partial t} = F_D\left(\overrightarrow{u} - \overrightarrow{u}_p\right) + \frac{\overrightarrow{g}\left(\rho_p - \rho\right)}{\rho_p} \tag{10}$$

where $F_D(\overrightarrow{u} - \overrightarrow{u_p})$ is the drag force per unit particle mass and

$$F_D = \frac{18\mu\, C_D \mathrm{Re}}{24\rho_p {d_p}^2} \tag{11}$$

where C_D is the drag coefficient, Re is the Reynolds number, and μ is the viscosity. The temperature of particle T_p, convective heat transfer, and the absorption/emission of radiation of the particle surface are related by the following equation.

$$m_p c_p \frac{dT_p}{dt} = hA_p\left(T - T_p\right) + \varepsilon_p A_p \sigma\left({T_R}^4 - {T_p}^4\right) \tag{12}$$

where h is the heat transfer coefficient, A_p is the particle surface area, and T_R is the radiation temperature which is used for estimating the radiative heat flux (black body temperature).

2.2. Drying model

The current simulation is based on the ANSYS fluent [27] theory in the drying process which takes place at the early stages of the gasifier when biomass is fed from the top. For the drying process, ANSYS employs two models, the Lee model [28], and Phase-Change model. However, in the current simulation, the Lee model is more relevant because it is used for mixtures, multi-phase VOF, and Euler-Lagrangian models. The liquid vapour mass transfer in such system is governed by the vapour transport equation (13):

$$\frac{\partial}{\partial t}\left(\alpha_v \rho_v\right) + \nabla\left(\alpha_v \rho_v \overrightarrow{V_v}\right) = \dot{m}_{lv} - \dot{m}_{vl} \tag{13}$$

Where v denotes the vapour phase, α_v is the volume fraction of vapour, $\dot{m}_{lv}$, and $\dot{m}_{vl}$ are the mass transfer rates due to drying (evaporation) and condensation respectively (kg/s/m^3).

2.3. Volatiles break-up approach and biomass decomposition

Due to the temperature rise in the oxidation zone, biomass goes through the drying process first, which allows all moisture to vaporize [29]. Biomass after drying decomposes into volatiles and char, and then these components further react with each other to form char and volatiles again, as discussed earlier ([5,30], and [31]). Volatiles break up approach in this work depends on an equilibrium model as shown in equation (14), and (15).

$$Biomass \rightarrow Volatiles + moisture + Tar + Char + ASH \tag{14}$$

$$Volatiles \rightarrow x_1\ CO + x_2 CO_2 + x_3 CH_4 + x_4 H_2 \tag{15}$$

Volatiles contain gases (CO, CO_2, CH_4, H_2, and H_2O), besides other hydrocarbons and tar. The devolatilization process however depends on the biomass composition (as determined by the ultimate and proximate analysis data) which also shows the volatiles and ash content.

Based on the volatiles' ultimate analysis data which are calculated from Refs. [1,27], an elemental mass balance is carried out to calculate the mole fraction of every species. The model, proposed by Ref. [32], calculates the mass fraction of every species produced during biomass pyrolysis based on temperature and the CO concentrations. Other gas species are calculated form the mass balance between the volatiles and pyrolysis products. The biomass break-up reaction (14) along with the volatile decomposition (15) are included in ANSYS code to start the simulation process.

As the tar evolution and formation kinetics during the pyrolysis zone is not previously studied, the current model will depend on a reported correlations from previous studies. Tar formation begins at the pyrolysis zone, and the tar species formation depends on the mass empirical relation developed by Ref. [25] based on the experimental results of [21]. They report the mass yield of tar species in g/kg of biomass. More details about the model can be found in Ref. [23].

Tar species different mass yields (g/kg of biomass) is reported by the following equation.

$$Y = aT^2 + b\,T + c \tag{16}$$

While the a, b, and c values are presented in Table 1.

After pyrolysis, the gas composition of volatiles and tar species are fed automatically to the next stages (oxidation and reduction) depending on their reactions (Tables 1 and 2).

2.4. Gas phase and char surface reactions

The set of reactions used to represent the oxidation and reduction processes are based on the recommendations of [6], (Table 2, and Table 3). The current model is further enhanced by implementing the detailed chemical reactions of tar species formation and evolution starting with devolatilization, oxidation and reduction, Table 4. All of the reactions, including the tar kinetic reactions, have been implemented in the ANSYS code in both the oxidation and reduction zones. Tar was initially assumed as one compound, but it was later classified into four main species (benzene, naphthalene, toluene, and phenol). Nine additional reactions have been added to the CFD code to incorporate the tar evolution, formation, and cracking along the gasifier.

2.5. Boundary and operating conditions

Two different feedstocks are used for model validation (Table 5) aiming to investigate the effect of gasifier operating conditions on the producer gas quality. Rubber wood and neem with their ultimate and proximate analysis data used for the initial model validation are illustrated in Table 5, while the boundary conditions used in the model are illustrated in Table 6. Both feedstocks were used previously in the kinetic model and in experiments, so it is a logical choice to use the same feedstocks for validation of CFD results.

Biomass is fed from the top of the gasifier as a mass flow rate input boundary condition, while the total number of particles are tracked through the Lagrangian approach (Discrete phase). Discrete phase model (DPM) follows the Euler-Lagrange approach where one phase representing fluid is solved by the Navier-Stokes equations, while the second phase representing dispersed particles is solved by tracking the specific number of particles through the flow field. Both the phases exchange mass, momentum, and energy with each other. The number of particles dispersed due to turbulence, is predicted by using stochastic tracking model (i.e., random walk model). At every time step, 1450 particles with a diameter of 0.355 mm are tracked. The model considers the effect of turbulence on the particles' trajectories (i.e., tries) which are injected into each cell of the computational mesh of the gasifier inlet [27]. The DPM proved to have good stability and better prediction for biomass gasification as demonstrated in the previous studies, e.g. see Refs. [42–45], and [46].

Table 1
Correlations for pyrolysis products [25].

	a	b	c
C_6H_6	−0.0003	0.7017	−387.6
$C_{10}H_8$	−0.0001	0.218	−115.32
C_7H_8	-6E-5	0.10701	−48
C_6H_6O	2E-5	−0.068	46.42

Table 2
Oxidation reactions.

	Reactions	A	*E* (kJ/mol)	*T*. exponent	Ref.
1	$2C + O_2 \rightarrow 2CO$	147,000	112.99	1	[33]
2	$CO + 0.5O_2 \rightarrow CO_2$	1.0e+10	126	0	[34]
3	$2H_2 + O_2 \rightarrow 2H_2O$	2.2e+09	109	0	[34]
4	$CH_4 + 2O_2 \rightarrow CO_2 + 2H_2O$	4.4e+11	126	0	[35]

Table 3
Reduction reactions.

	Reactions	*A*	*E* (kJ/mol)	*T*. exponent	Ref.
5	$C + CO_2 \rightarrow 2CO$	8.268	188.2	1	[33]
6	$C + H_2O \rightarrow CO + H_2$	42.5	142	1	[33]
7	$0.5C + H_2 \rightarrow 0.5CH_4$	8.8894e-06	67.16	1	[33]
8	$CH_4 + H_2O \rightarrow CO + 3H_2$	3e+08	125	0	[34]
9	$CO + H_2O \rightarrow CO_2 + H_2$	2.35e+10	288	0	[36]
10	$CO_2 + H_2 \rightarrow CO + H_2O$	1.785e+12	326	0	[36]

Table 4
Reactions of tar species implemented in the model.

	Reactions and rate expression	*A* (s^{-1})	*E* (kJ/mol)	Ref.
11	$C_7H_8 \rightarrow 0.17C_{10}H_8 + 0.89C_6H_6 + 0.67H_2$ $r_1 = k_1 [C_7H_8]$	2.23E13	315	[37]
12	$C_{10}H_8 \rightarrow 10\,C + 4H_2$ $r_2 = k_2 [C_{10}H_8]^2 [H_2]^{-0.7}$	5.56E15	360	[38]
13	$C_{10}H_8 + 4H_2O \rightarrow C_6H_6 + 4CO + 5H_2$ $r_3 = k_3 [C_{10}H_8] [H_2]^{0.4}$	1.58E12	324	[38]
14	$C_7H_8 + H_2 \rightarrow C_6H_6 + CH_4$ $r_4 = k_4 [C_7H_8] [H_2]^{0.5}$	1.04E12	247	[38]
15	$C_6H_6 + 5H_2O \rightarrow 5CO + CH_4 + 6H_2$ $r_5 = k_5 [C_6H_6]$	4.4E8	220	[38]
16	$C_6H_6 + 7.5\,O_2 \rightarrow 6CO_2 + 4H_2O$ $r_6 = k_6 [C_6H_6]^{-0.1} [O_2]^{1.25}$	17.83	125.5	[38]
17	$C_6H_6 + 3O_2 \rightarrow 6CO + 3H_2$ $r_7 = k_7 [C_6H_6] [O_2]$	1.58E15	202.6	[38]
18	$C_7H_8 + 9\,O_2 \rightarrow 7CO_2 + 4H_2O$ $r_8 = k_8 [C_7H_8]^{-0.1} [O_2]^{1.25}$	14.26	125.5	[38]
19	$C_6H_6O \rightarrow CO + 0.4C_{10}H_8 + 0.15\,C_6H_6 + 0.1CH_4 + 0.75H_2$ $r_9 = k_9 [C_6H_6O]$	1.0E7	100	[25, 39]

Table 5
Feedstocks' data used in validation.

	Ultimate analysis db. (%)				Proximate analysis db. (%)			
	C	H	O	N	Vol.	FC	Ash	MC
Rubber wood [40]	50.6	6.5	42	0.2	80.1	19.2	0.7	18.5
Neem [41]	45.1	6.0	41.5	1.7	81.75	12.65	5.6	10

Db – on dry basis.

Table 6
Boundary conditions used in validation.

	Rubber wood	Neem
Equivalence ratio	0.326	0.3
$\dot{m}_{fuel}$, kg/hr	0.316	0.694
$\dot{m}_{air}$, kg/hr	0.631	1.142
Air *T* (K)	600	600
Biomass *T* (K)	300	300
Gauge *P*, producer gas outlet	0	0

2.6. Numerical simulation and convergence testing

The governing equations of two phases are numerically solved by using an implicit finite volume method. A pressure velocity coupled algorithm is used where it encompasses a coupled solution for the momentum and pressure-based equations. This solving criterion gives higher rate of solution convergence [27]. The spatially discretised pressure equation is solved by PRESTO (PREssure STaggering Option) method, which is a default option for multiphase simulations or volume of fluid (VOF) models with mixtures or having more than one fluid in the system. The PRESTO scheme is more applicable for the models as it gives better solution convergence. Energy, momentum, gas species, and discrete ordinates under the spatial discretization uses a second order upwind scheme for more accurate and stable solution. Convergence criteria for residuals is set as default, where all the relaxation factors are set to 10^{-3} while for the energy and discrete ordinate radiation are set to 10^{-6} to again ensure the stable accurate solutions. The particles are tracked cell by cell through the control volume, where the devolatilization, combustion and gasification take place according to the specified rate reactions. The overall solution methods and residuals control are concluded in Table 7.

3. Results and discussion

3.1. Mesh dependency and model validation

Mesh independency test is performed first by using five different mesh sizes with the cell numbers of 22,320, 39,744, 90,770, 203,980, and 319,780 respectively. Producer gas composition along with the higher heating value of rubber wood gasification is shown in Fig. 2. The results show a slight variation in the gas compositions for all the grids employed. For example, the CO concentration varies between 20.9 and 20.4 in vol% when the grid size is changed from 203,980 to 22,320 – a variation of only less than 2%. Also, the variation in both CO_2 (9.11–9.5) mol% and CH_4 (1.8–2.17) mol.% for the same grids is insignificant. Additionally, the higher heating value (HHV (MJ/Nm^3)) does not differ much (5.8 and 5.74 MJ/Nm^3) for the grid numbers 90770 and 203,980. However, starting with the 90,770 cells, the overall gas composition appears to be stable with negligible variations, and the heating value also almost remains the same. As a result, the mesh size of 90,770 is selected for the further simulations presented in the current work, as higher mesh density is time consuming and will require higher computational costs.

Fig. 3 depicts the results of CFD modelling for the two feedstocks as well as a comparison with the experimental, and kinetic modelling results [5]. Rubber wood was gasified at an ER of 0.326 and an MC of 18.5% [40], while neem gasification was at an ER of 0.3 with an MC of 10% [41]. The results show the volume (%) of dry gas composition at the gasifier outlet for the three data sets. Based on the comparison, the CFD results of both feedstocks show good agreement for all the gas compositions with those of the kinetic code and the experiments. A negligible variation in all the gas species formation is found and the results for the CFD, experiment and kinetic code results vary between 8 and 13 vol%, and 6 and 14 vol% for rubber wood and neem respectively, demonstrating the model's suitability to simulate the process of downdraft biomass gasifiers.

Tar species produced during the gasification of a wood sample at an

Table 7
Solution methods followed in the CFD modelling.

Phases	Euler-Lagrangian
Models included	Turbulence model: k-epsilon 2 equations Radiation: Discrete ordinates Species Transport for Finite rate/Eddy transport kinetic model Intensity and Hydraulic Diameter specification
Solution methods	Pressure-velocity coupling, Coupled Momentum and Energy: 2nd order upwind discretization scheme Pressure discretization scheme, PRESTO
Residuals' level	10^{-3} for all variables, for Energy and radiation 10^{-6}

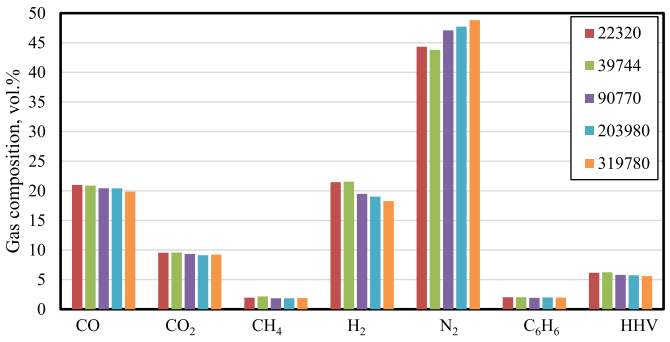

Fig. 2. Producer gas composition vol. %, and HHV (MJ/Nm^3) at different mesh sizes.

ER of 0.35 and an MC of 10% are presented in Fig. 4. Comparisons are shown between the results of the CFD model, kinetic model and the corresponding experiment [23]. Note that all the tar results have been converted from μg/100 ml of the produced gas to the unit of g/Nm^3 for easy tracking and comparison with the experimental or numerical data, as this unit is widely used in the literature in quantifying and estimating tar produced in gasification. The results in Fig. 4 show that all the major tar species produced, and the total tar amount are in fairly good agreement. A negligible decrease in the CFD model prediction for the total tar amount is found because of a very slight amount of benzene prediction. The kinetic model slightly outperforms when comparing with the CFD predictions for tar production. However, the CFD results are still matching with the experimental data with a small deviation for the different species and total tar amount produced. Furthermore, one of the main research aims is to study the hydrodynamics of tar and gas species within the gasifier which is not applicable for the kinetic models. The following discussions (Figs. 5–12) will present the distribution of velocity, temperature, reaction rates, volatiles decomposition across the gasifier height. As a result, the CFD is a strong numerical procedure that overcomes the limitations of such kinetic models. Phenol concentrations are too low and can be considered as negligible compared to the other species because, and it is a primary tar compound that tends to be fully cracked and converted to the other tar species at higher temperatures. Based on the kinetic and CFD models, the phenol concentration is zero, while from the experiments it is reported as <0.02 g/Nm^3 (thus negligible).

Furthermore, benzene and naphthalene show fairly well agreement with both the experimental and kinetic code results. Both compounds have the highest portion of tar produced during the biomass gasification, accounting more than 60% of the tar produced in most cases ([22,47], and [1]). Toluene concentration from the CFD model shows slightly lower than that of the experiment or kinetic model. However, it meets a strong agreement with the other data.

3.2. Rates of reactions with an effect of ER

Fig. 5 illustrates the reaction rate of volatiles and the mass fraction of volatiles along gasifier centreline for rubber wood gasification at ER = 0.326, and MC of 18%. After drying, the decomposition of biomass to volatiles takes place at the pyrolysis zone and the very early stages of the

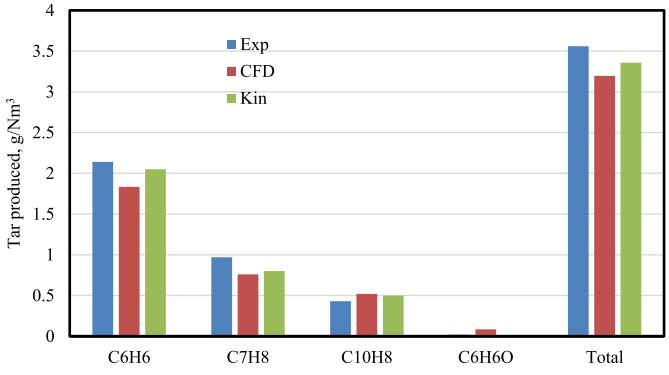

Fig. 4. Detailed tar species validation.

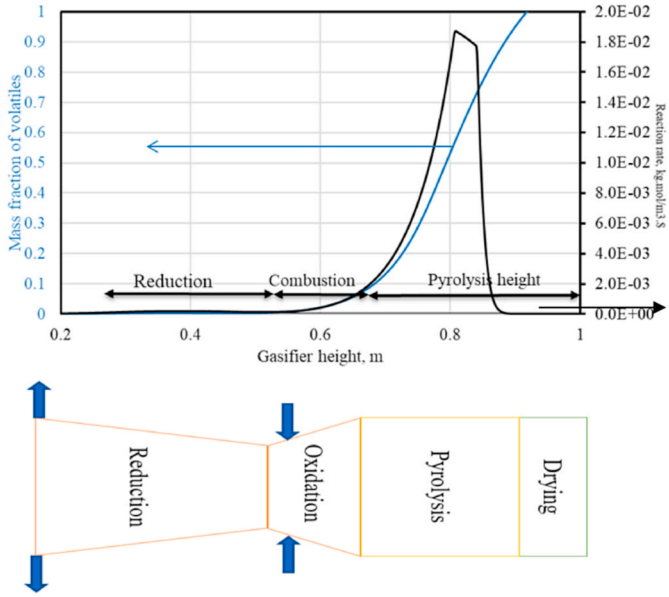

Fig. 5. Volatiles' reaction rate (right), and decomposition (left) along the gasifier height.

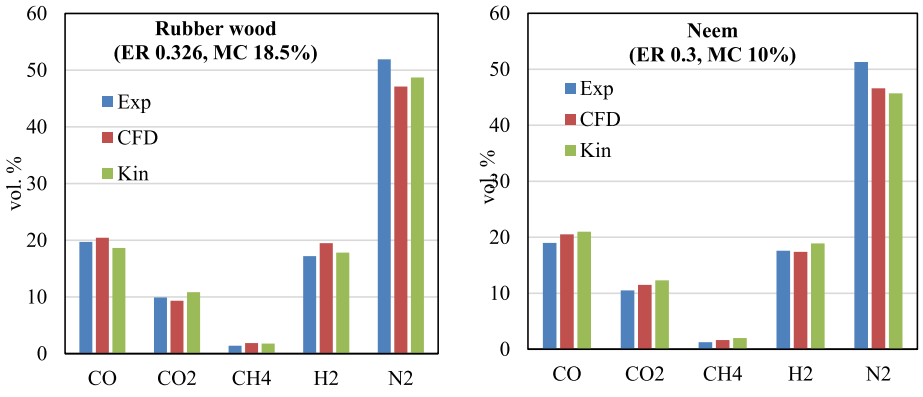

Fig. 3. Rubber wood and neem comparison (Producer gas compositions in vol %).

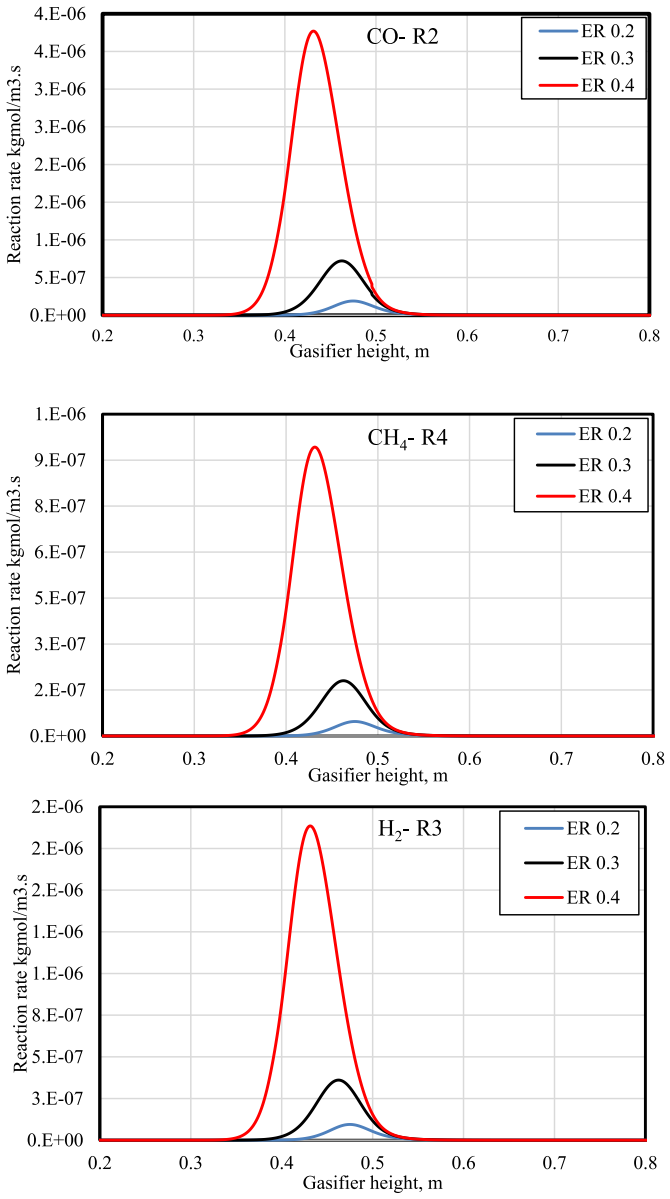

Fig. 6. Combustion reactions rates along the gasifier centreline at different ERs.

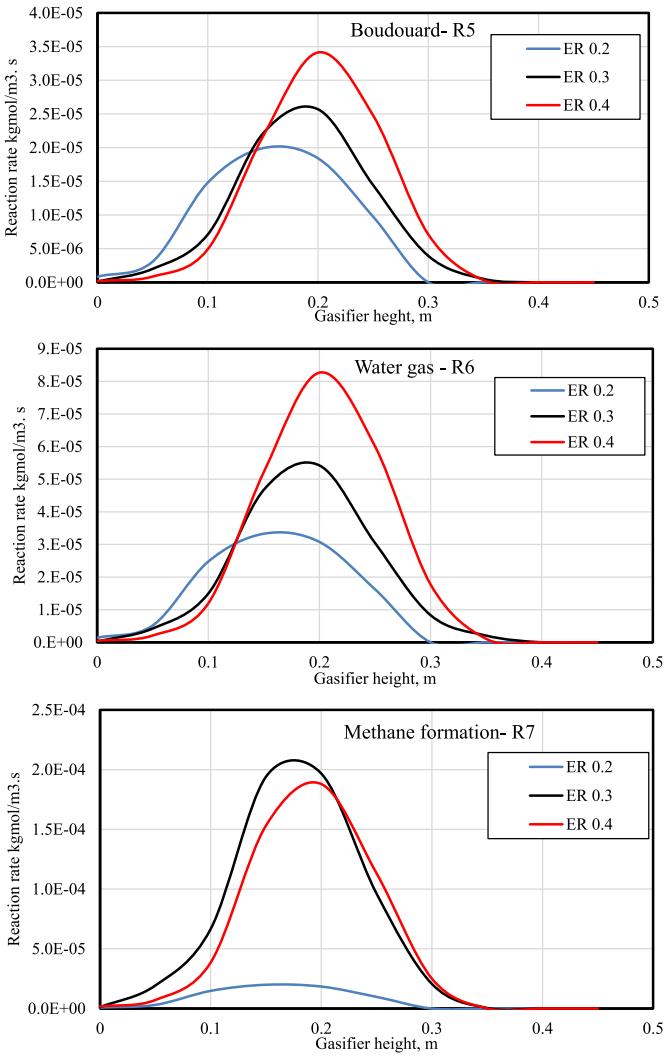

Fig. 7. Gasification reaction rates along the gasifier for different ERs.

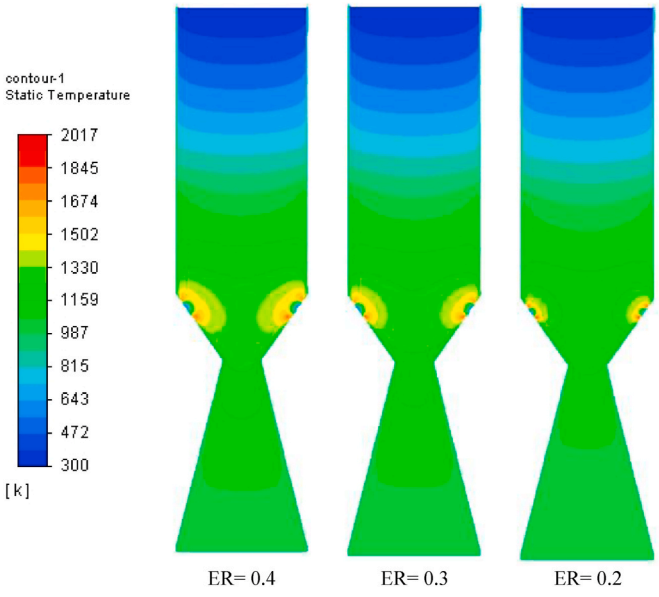

Fig. 8. Temperature contours along the gasifier with different ERs.

combustion zone. Biomass devolatilization rate reaches its peak in the middle of the pyrolysis zone, and then gradually decreases as biomass is fed into the combustion zone, until it reaches zero just above the oxidation zone (i.e., at about 60 cm height of gasifier) where the other reactions occur. Biomass decomposition into char, tar, and gases takes place in the pyrolysis zone as also clearly shown in the figure. The mass fraction of biomass decomposition starts at 1 until it approaches 0 at the onset of combustion, as demonstrated by the drop in the decomposition rate towards the end of the pyrolysis zone. It is also found that changing ER has no effect on decomposition because no air is driven within the pyrolysis zone. As a result, ER has no effect on the behaviour of pyrolysis products. The findings meet strong agreement with previous experimental and numerical results e.g., ([6,44]).

The oxidation zone is where the combustion reactions take place, as seen in Fig. 6. The reaction rates of CO, CH_4, and H_2 combustion are examined for rubber wood gasification at ERs of 0.2, 0.3, and 0.4. The oxidation reactions are exothermic, generating the heat required for all the other reaction processes of gasification such as biomass decomposition in pyrolysis and reduction reactions in the gasification zone. All of the combustion reactions, as also shown in this figure, take place in the

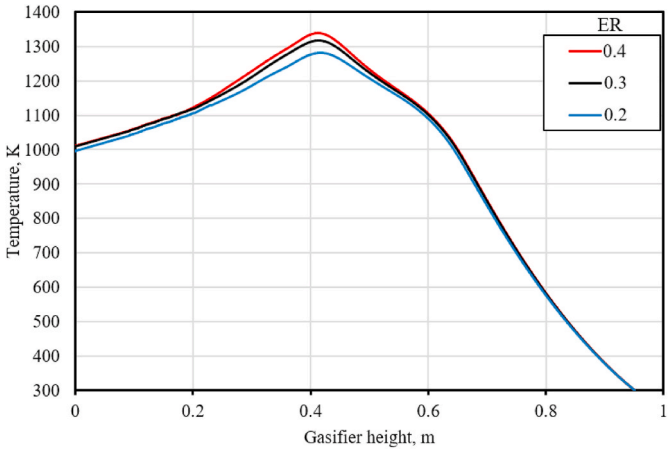

Fig. 9. Temperature distribution at different ERs along the gasifier centreline.

oxidation zone between the gasifier heights of 35 and 50 cm. A higher combustion rate is found for CO followed by H_2 and CH_4 as clearly illustrated in the figure. This is due to the increased amounts of CO produced during pyrolysis followed by H_2, and CH_4 respectively. Additionally, the smaller activation energy for H_2 combustion compared to CO combustion leads to decrease its combustion rate (Table 1).

In the same figure, the effect of changing ER on the reaction rates and the formation of different species is also presented. As the ER increases from 0.2 to 0.4, the reaction rates increase, and the corresponding peak is shifted towards the middle of the combustion zone. Higher ERs tend to increase the amount of air (O_2) inside the oxidation zone, and consequently, increase the rate of reactions based on the combustion reaction rates (Table 1). Furthermore, increased air inside the gasifier favours flow turbulence leading to increase in the temperature and corresponding rates of oxidation reactions. The highest reaction rate is usually formed at the middle of combustion zone (~0.42 m height). It was found that the highest reaction rate for CO combustion (R2- Table 1) is $3.7*10^{-6}$ kgmol/m^3s at ER 0.4, while the lowest value is $4.7*10^{-8}$ kgmol/m^3s at ER 0.2 for CH_4 combustion (R4- Table 1). Such findings strongly align with those reported in Ref. [6].

The set of results in Fig. 7 further illustrate the reaction rates taking place in the reduction zone are the boudouard, water-gas, and methane formation reactions, respectively (R5,6,7- Table 2). Rubber wood is used as a feedstock at a fixed MC of 18.5% with varying ER. As seen from the figure, all the specified reactions take place in the reduction zone where it starts at around 35 cm from the gasifier height and proceeds towards the end of the gasification zone. The methane formation reaction has the highest reaction rate, followed by the water-gas and boudouard reactions – the findings also strongly agree with those reported in Ref. [6]. It is also worth further noting that all the reactions initiate near the end of the combustion zone, with only a very small rate possibly occurring in the combustion zone. The boudouard reaction has the lowest reaction rate due to the consumption of CO_2 to CO. This is mainly because CO_2 is a very stable compound and requires heat to be converted to other species ([21], and [1]) because it is strongly endothermic and requires heat to be initiated. These results are, again, consistent with the previously published work, which states that the reduction reactions are mostly endothermic thus require heat to occur [48].

Furthermore, while the methane formation reaction shows high reaction rates, it is mainly dependent on the amount of CH_4 which is mostly found in small amounts during the gasification process. Reaction 7, on the other hand, which show lower amounts of CH_4 because of its low activation energy and also its dependency on C, and H_2 formation along the reduction zone. Yet, it is effective in predicting the accurate amount of CH_4 formation during the process of gasification. Lower ER (0.2) tends to produce higher reaction rates for the boudouard, and methane formation reactions as illustrated in the figure. This is because lower ER in the combustion zone tends to produce higher concentrations of CO, and CH_4 and as a result, the formation rate is increased. Unlike the water gas reaction, which depends on the amount of steam present inside the gasifier. For higher ER, H_2 combustion reaction takes place (Fig. 6), leading to more steam formation, and consequently, increasing the rate of formation of water-gas reaction.

The combustion (gas-phase) reactions rates are defined based on a volumetric basis in which the creation/destruction rates of the different species are a source term in the species transport equation (eqn. (7)). While this is the case in most combustion reactions, the gasification reactions mostly depend on the char amounts, and are defined as a particle surface reaction in which, the rate of formation of different species is governed by the diffusion and chemical kinetics within the surface [27]. As a result, the surface reactions create sinks and sources of the different species within the gas phase, and on the reacting species surface [49].

3.3. Temperature distribution inside the gasifier

The equivalence ratio and air amount injected into the gasifier play a critical role in the producer gas production, chemical reactions, temperature and in fact, the whole gasification process. Hence, studying the effects of changing ER on the gasification temperature and other parameters will lead to the further understanding of its effect on gasification, resulting in higher producer gas production and gasification process efficiency.

Fig. 8 depicts the temperature contours inside the gasifier for rubber wood gasification at the different equivalence ratios and a fixed MC of 18.5%. The results clearly illustrate that the higher temperature is predicted in the oxidation zone, followed by the reduction and pyrolysis zones. The peak temperature, or in other word the ignition temperature, (1900–2015) K is seen near the air injection points; however, it is not the combustion temperature, as the temperature drops to normal levels (~1400K) in the middle of the gasifier, Fig. 8. As the ER increases, the temperature inside the gasifier also increases. This is due to increased air injection and turbulence inside the gasifier, which increases the reaction rates for the heterogeneous combustion reactions.

Further in Fig. 9, the temperature profile along the gasifier centreline is compared for the different ERs. As clearly shown in the figure, more air addition from a higher ER tends to increase the temperature inside the gasifier. The maximum temperature for ER of 0.4 was found to be around 1340K. The change of ER shows a negligible difference in the pyrolysis temperature. This is because pyrolysis temperature depends on the feedstock type, and moisture levels. Since both are fixed, (rubber wood. 18.5% MC), it is expected to have fixed pyrolysis temperature ~700 K. On the other hand, ER affects the amount of air/oxidant injection inside the combustion zone. Higher ERs, with high oxygen, lead to an increase in turbulence mixing as well as in the heterogenous oxidation reaction rates (Table 2). Thus, resulting in the higher temperatures and heat release in the combustion zone. This has been also demonstrated in Fig. 8, where higher temperatures are found for higher ERs. The resulting gasification/reduction temperatures also depend on ER as illustrated by (Figs. 8, and Fig. 9).

However, when ER decreases, the temperature decreases as well. The temperature rise with ER is also in good agreement with the previous works ([31], and [40]) as well as with the results derived from the kinetic model [5].

3.4. Tar species formation

Tar evolution in the pyrolysis zone is described using a mass yield relation [32]. In the combustion and gasification zones, the tar species formation depends on the detailed reaction rate kinetics [37], and [38]. The CFD model is used to investigate the formation of the different species of tar along the gasifier in both steady and unsteady states, as well as the effect of residence time on the formation and destruction of

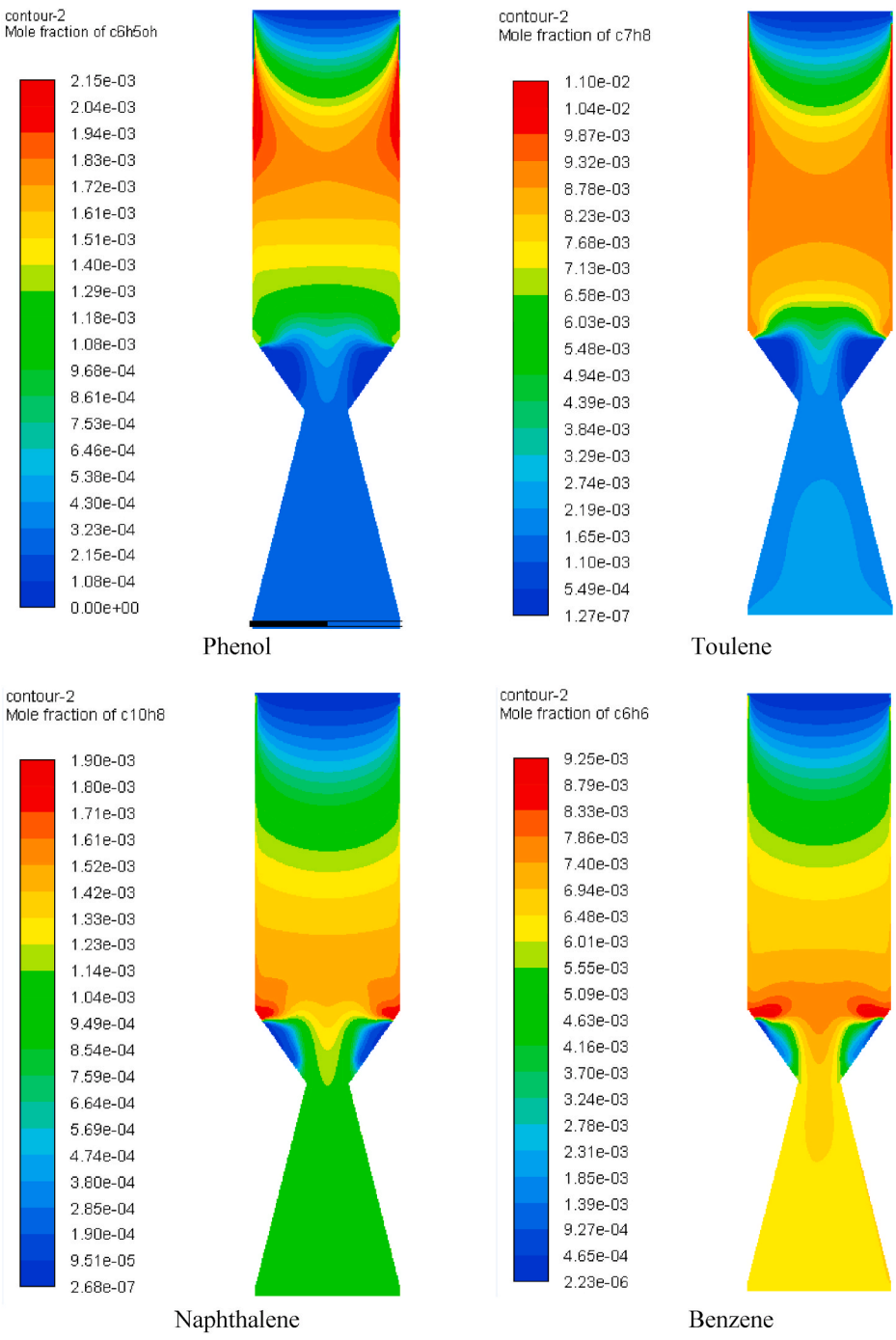

Fig. 10. Various tar species mole fraction contours inside the gasifier.

various species.

3.4.1. *Tar species distribution inside the gasifier*

Phenol concentrations in the producer gas are usually close to zero and can be neglected, as evidenced in Fig. 10. In the early stage of pyrolysis, a large amount of phenol is formed; but as the temperature increases, it reacts more with the other compounds and eventually converts to other forms. When the temperature is high enough during gasification, it also tends to decrease gradually, and in some cases, it tends to be fully consumed and converted to benzene, naphthalene, and other gas species (CO, H_2, and CH_4).

Toluene formation inside the gasifier has the same trend as phenol, with a higher concentration in the pyrolysis zone followed by destruction in the oxidation and reduction zones, as also evidenced in Fig. 10. However, depending on the reduction reactions and temperature of the gasification zone, toluene starts reforming again in small amounts at the reduction zone. Although it needs further understanding and clarifications, this could be because of the reaction rates, backward reactions, and the complicated chemistry involved in such reactions. However, after reaching the steady state in the simulation, it appears that all of the phenol has been consumed (Figs. 10 and 11). Particularly, at temperatures above 773 K, the primary tars start to re-form ([48], and [47]) and convert to the secondary, and then the tertiary tars. The temperatures in the oxidation and reduction zones, that are higher than 1173 K, are enough to destroy the primary tar species and transform them into the other compounds.

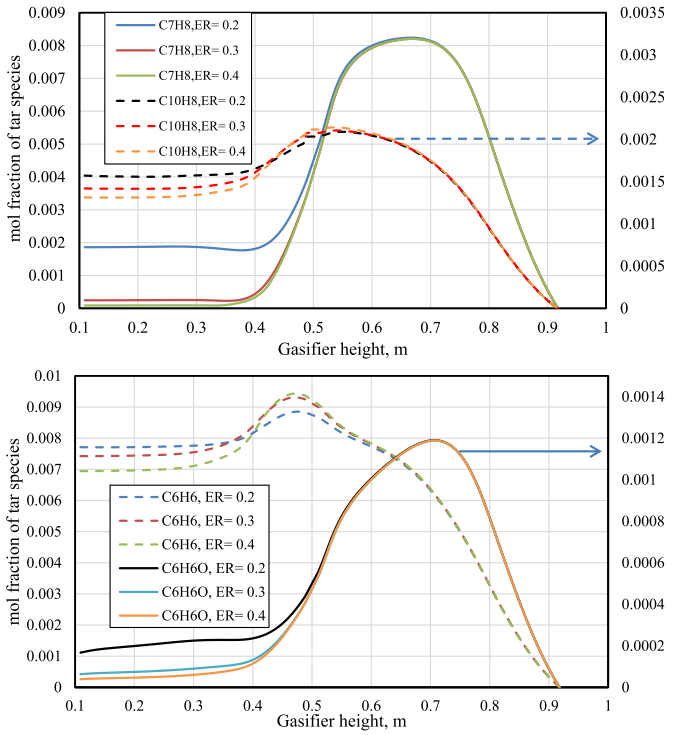

Fig. 11. Tar species distribution along the gasifier centreline with different ERs.

Nevertheless, unlike the other species, naphthalene formation shows a different trend. It is formed in considerable amounts in the producer gas as illustrated in Fig. 10. Small amounts are produced during pyrolysis because it is a tertiary tar which requires higher temperatures to present and form. Higher temperatures in the oxidation zone >1300K are favourable for the naphthalene formation and total conversion at 1600 K [22]. Further, based on the tar kinetic reactions, naphthalene is also converted to char, H_2, CO and benzene. Those reactions occur in both the combustion and reduction zones; however, it is more likely to happen in the reduction zone because of the presence of water vapour.

Benzene has the highest portion of tar species, which is usually greater than 37% from the weight of the total tars produced [1]. Benzene starts forming in pyrolysis and followed by a slight decrease in oxidation but increases again in the reduction zone. Oxidation reactions destroy benzene and convert it to CO, CO_2, CH_4, H_2 and H_2O. However, benzene is still found in larger amounts compared to the other tar species, and during oxidation it is slightly cracked. This is because of its higher stability than the other tar species, and hence it forms as the highest portion of tar compounds during the gasification process [1]. Furthermore, benzene requires a very high temperature to crack (1400–1700) K [22]. On the other hand, these reactions (benzene combustion R16, 17) depend on oxygen amount and have slow reaction rates. As a result, it is unlikely that they will take place in the oxidation zone or will never happen in the reduction zone where no oxygen is present. Whereas the other tar species (phenol, naphthalene, and toluene) are converted to benzene and other compounds at this temperature range. All the previous factors, therefore, tend to increase the amount of benzene along the gasifier height as the temperature increases, which further agrees with the results of [20].

Tar species formation along the centreline is illustrated in Fig. 11. The results follow the same trend described earlier in Fig. 10. That is, in the pyrolysis zone, phenol shows higher concentration; this is because it is a primary tar compound and usually formed in higher amounts during the devolatilization process and has been further transformed into the secondary and tertiary tars during combustion and gasification. At the gasifier exit, benzene shows the highest portion of tar species followed

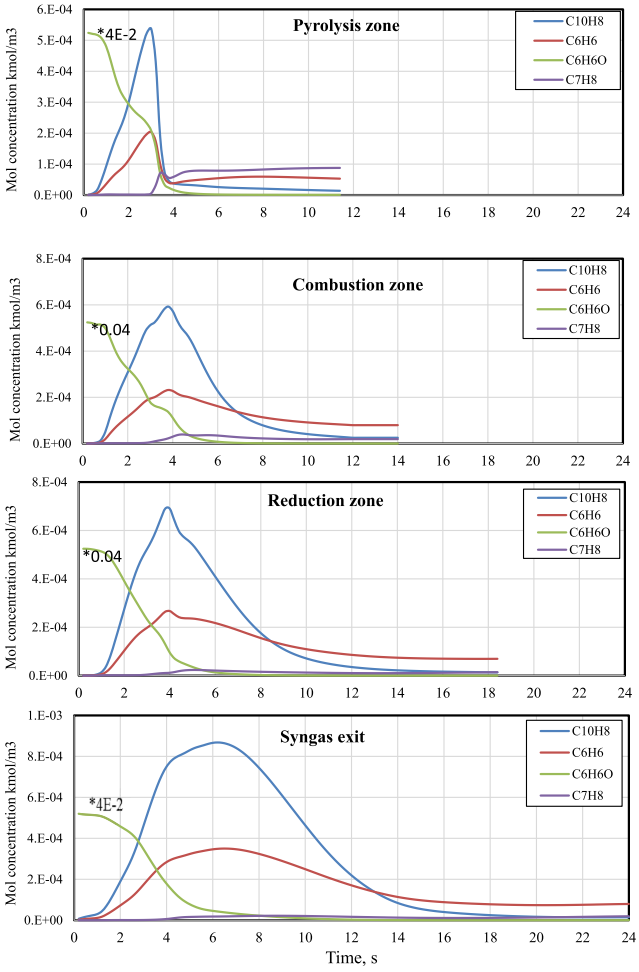

Fig. 12. Temporal distribution of tar species at the middle point of different zones, and gasifier exit.

by toluene and naphthalene, while phenol shows negligible values at the exit of the gasifier, as expected. Poly aromatic hydrocarbons (PAH) are favourable to be formed during high temperature. However, it was stated that benzene, and naphthalene are found in large amounts during the process pyrolysis [50], and [51]. Benzene and naphthalene are more affected by the temperature rise and therefore show higher conversion rates in higher temperature [52]. However, the formation of naphthalene was found in considerable amount (although small) in the pyrolysis zone at around 0.7 m height of the gasifier. At this height, the temperature was around 800–900 K (Fig. 7) and at this temperature level, naphthalene could be found at considerable amounts as stated in the experimental and numerical study of [52].

Additionally, for all the species, the ER has a strong effect on their formation and destruction. Higher ER always shows smaller amounts of tar species at the gasifier exit. This is because higher temperature and turbulence inside the gasifier favour tar destruction, and therefore, lower amounts of tar. It is also noticed that all species amounts tend to be similar at the pyrolysis zone, because there is no effect of ER on either tar or volatiles at this stage (discussed earlier in Fig. 5).

3.4.2. *Temporal evolution of tar species*

Unsteady simulations are also performed to study the formation of different tar species over time, starting with the evolution at pyrolysis and transformation through oxidation and gasification, and producer gas exits (Fig. 12). The transient state is examined for 24 s with a time step of 0.05 s, A well understanding of the tar formation and its nature is the primary requirement that would help to decrease the tar amounts

produced with producer gas. Therefore, all the simulation results of tar species presented below are processed at the mid-location of every zone, while they are face averaged at the gasifier exit.

The evolution of tar species at the pyrolysis zone over time is shown in Fig. 12. All the species, except for phenol, start to increase and reach their peaks at different time, and then decrease and eventually stabilise after 6 s. Phenol concentrations were found to be very high at the beginning, so the phenol was multiplied by 0.04 for an easy illustration in the chart area. Phenol concentrations are found to be very high because of its nature being a primary tar, which forms at pyrolysis, then over the time and when the temperature inside the gasifier increases, it starts to crack and convert to other higher tar compounds and consequently, tends to decrease by the end.

On the other hand, toluene was found to have the highest portion of tar species at the pyrolysis end, which is consistent with the previous and present research findings. Toluene being the most stable primary tar is formed at usual pyrolysis temperatures but cracks and converts to benzene and naphthalene at higher temperatures of the oxidation zone. Benzene is present in considerable amounts, while naphthalene in lower amounts as a PAH that needs higher temperatures to form. At the combustion zone, the results start to stabilise after 11 s, which should be longer than the pyrolysis duration (6 s). That is due to the fact that species begin to form during pyrolysis and then go through the combustion zone which takes time to stabilise. All the species exhibit the similar trend as those identified in the pyrolysis zone. However, benzene and naphthalene are formed in greater amounts, because of the higher combustion temperatures (Fig. 7) that crack the primary tar molecules and convert them to the secondary and tertiary tars. Toluene is found in small amounts while phenol is fully consumed because of the higher temperature at the oxidation zone.

The results have a logical trend, where the sum of the tar contents (in $kmol/m^3$) at the end of pyrolysis ($16*10^{-5}$) and combustion ($13*10^{-5}$) decreases. Additionally, the results show that the primary tars are formed during pyrolysis (e.g. toluene $\sim 8.8*10^{-5}$), while at the end of oxidation benzene (tertiary tars) has the highest portion ($8.5*10^{-5}$) followed by naphthalene and toluene, which agrees strongly with the previous studies published in the literature ([21,53], and [25]).

Tar species formation at the reduction zone start to stabilise after a longer time than combustion and pyrolysis, around 14 s. Tar species formation follows the same trend as in the combustion zone because of again the higher temperature. Finally, the average values of tar species evolution at the producer gas exits are presented in the same figure. The species formation takes longer than the other zones start to stabilise, around 18 s. Initially, phenol is found in large amounts, but it decreases or fully consumed over time and temperature rise. Benzene and naphthalene are formed in large amounts, then they cracked slightly as the temperature increases. While toluene, being a stable compound, stabilises early and is found in considerable amounts. Eventually, benzene is the highest portion of tar species formed, followed by toluene, naphthalene, and phenol in a very small amount. The results are matching with the findings illustrated earlier in Fig. 9.

4. Conclusions

A CFD model was developed for the investigation of the evolution and formation of major tar species in a downdraft gasifier. Tar representatives included benzene, naphthalene, toluene, and phenol which were classified as primary, secondary, and tertiary tars. The results of the producer gas composition as well as tar species formations were validated with the kinetic modelling and experimental data.

Detailed reaction kinetics were investigated at varying ER from 0.2 to 0.4, revealing the rates of reactions for various producer gas and tar species. The highest reaction rate was found for CO combustion at ER 0.4, while the lowest rate was for CH_4 combustion at ER 0.2. On the other hand, the boudouard reaction has the lowest reaction rate, while the methane formation reaction has the highest reaction rate.

Furthermore, the unsteady tar distribution at the pyrolysis, combustion, and reduction zones revealed that the primary tars formed in their higher concentration during pyrolysis. These were then consumed at the oxidation zone, and subsequently reduced at the reduction zone. On the other hand, the tertiary tars were formed initially with smaller amounts at pyrolysis, consumed at oxidation, but reformed again at reduction because of the conversion of the primary tars into the secondary and tertiary tars. The results further demonstrated that the tar species were stabilised after 6, 11, 14, and 18 s in pyrolysis, combustion, reduction, and gasifier exit respectively.

Data availability

Data will be made available on request.

References

[1] P. Basu, Biomass Gasification, Pyrolysis, and Torrefaction. Practical Design and Theory, second ed., Academic Press, Amsterdam, 2013.
[2] A.M. Sepe, J. Li, M.C. Paul, Assessing biomass steam gasification technologies using a multi-purpose model, Energy Convers. Manag. 126 (2016) 216–226.
[3] J. Li, M.C. Paul, K.M. Czajka, Studies of ignition behaviour of biomass particles in a down-fire reactor for improving co-firing performance, Energy Fuel. 30 (7) (2016) 5870–5877.
[4] A.M. Salem, U. Kumar, A.N. Izaharuddin, H. Dhami, T. Sutardi, M.C. Paul, Advanced numerical methods for the assessment of integrated gasification and CHP generation technologies, in: Coal and Biomass Gasification, Energy, Environment, and Sustainability, Springer, 2018, pp. 307–330.
[5] A.M. Salem, M.C. Paul, An integrated kinetic model for downdraft gasifier based on a novel approach that optimises the reduction zone of gasifier, Biomass Bioenergy 109 (2018) 172–181.
[6] U. Kumar, M.C. Paul, CFD modelling of biomass gasification with a volatile break-up approach, Chem. Eng. Sci. 195 (2019) 413–422.
[7] Z.A. Zainal, R. Ali, C.H. Lean, K.N. Seetharamu, Prediction of performance of a downdraft gasifier using equilibrium modeling for different biomass materials, Energy Convers. Manag. 42 (12) (2001) 1499–1515.
[8] A.K. Sharma, Modeling and Simulation of a Downdraft Biomass Gasifier 1. Model Development and Validation, 52, Energy Conversion and Management, 2011, pp. 1386–1396.
[9] N. Bianco, M.C. Paul, G.B.E. Brownbridge, D. Nurkowski, A.M. Salem, U. Kumar, A. N. Bhave, M. Kraft, Automated advanced calibration and optimization of thermochemical models applied to biomass gasification and pyrolysis, Energy Fuel. 32 (10) (2018) 10144–10153.
[10] A.M. Salem, H.S. Dhami, M.C. Paul, Syngas production and combined heat and power from scottish agricultural waste gasification—a computational study, Sustainability 14 (7) (2022) 3745, https://doi.org/10.3390/su14073745.
[11] P.N. Sheth, B.V. Babu, Modeling and simulation of reduction zone of downdraft biomass gasifier: effect of char reactivity factor, Energy Convers. Manag. 47 (2006) 2602–2611.
[12] T.K. Patra, P.N. Sheth, Biomass gasification models for downdraft gasifier: a state-of-the-art review, Renew. Sustain. Energy Rev. 50 (2015) 583–593.
[13] U. Kumar, M.C. Paul, Sensitivity analysis of homogeneous reactions for thermochemical conversion of biomass in a downdraft gasifier, Renew. Energy 151 (2020) 332–341.
[14] T. Phuphuakrat, N. Nipattummakul, T. Namioka, S. Kerdsuwan, K. Yoshikawa, Characterization of tar content in the syngas produced in a downdraft type fixed bed gasification system from dried sewage sludge, Fuel 89 (2010) 2278–2284.
[15] D.F. Fletcher, B.S. Haynes, F.C. Christo, S.D. Joseph, A CFD based combustion model of an entrained flow biomass gasifier, Appl. Math. Model. 24 (2000) 165–182.
[16] L. Yu, J. Lu, X. Zhang, S. Zhang, Numerical simulation of the bubbling fluidized bed coal gasification by the kinetic theory of granular flow (KTGF), Fuel 86 (2007) 722–734.
[17] R. Gupta, P. Jain, S. Vyas, CFD modeling and simulation of 10KWE biomass downdraft gasifier, Int. J. Curr. Eng. Technol. 7 (4) (2017) 1446–1452.
[18] Y. Wu, Q. Zhang, W. Yang, W. Blasiak, Two-dimensional computational fluid Dynamics simulation of biomass gasification in a downdraft fixed-bed gasifier with highly preheated air and steam, Energy Fuel. 27 (6) (2013) 3274–3282.
[19] P.C. Murugan, S. Joseph Sekhar, Numerical simulation of Imbert biomass gasifier toSelect the feedstock available in remote areas, Environ. Prog. Sustain. Energy 36 (3) (2017) 708–716.
[20] C.M. Kinoshita, Y. Wang, J. Zhou, Tar formation under different biomass gasification conditions, J. Anal. Appl. Pyrol. 29 (1994) 169–181.
[21] A. Dufour, E. Masson, P. Girods, Y. Rogaume, A. Zoulalian, Evolution of aromatic tar composition in relation to methane and ethylene from biomass pyrolysis-gasification, Energy Fuel. 25 (2011) 4182–4189.
[22] A. Jess, Mechanisms and kinetics of thermal reactions of aromatic hydrocarbons from pyrolysis of solid fuels, Fuel 75 (12) (1996) 1441–1448.
[23] Ahmed M. Salem, Ilman Nuran Zaini, Manosh C. Paul, Weihong Yang, The evolution and formation of tar species in a downdraft gasifier: numerical modelling and experimental validation, Biomass Bioenergy 130 (2019).

[24] M.L.V. Rios, A.M. González, E.E.S. Lora, O. del Olmo, Reduction of tar generated during biomass gasification: a review, Biomass Bioenergy 108 (2018) 345–370.
[25] A. Dufour, L. Abdelouahed, O. Authier, G. Mauviel, J.P. Corriou, G. Verdier, Detailed modeling of biomass gasification in dual fluidized bed reactors under aspen plus, Energy Fuel. 26 (2012) 3840–3855.
[26] D.T. Pio, L.C.M. Ruivo, L.A.C. Tarelho, J.R. Frade, E. Kantarelis, K. Engvall, Tar formation during eucalyptus gasification in a bubbling fluidized bed reactor: effect of feedstock and reactor bed composition, Energy Convers. Manag. 229 (2021), 113749.
[27] ANSYS 15 Fluent Theory Guide, Canonsburg, PA 15317, 2013.
[28] W.H. Lee, A Pressure Iteration Scheme for Two-phase Modeling, Technical Report LA-UR 79-975, Los Alamos Scientific Laboratory, Los Alamos, New Mexico, 1979.
[29] C. Dejtrakulwong, S. Patumsawa, Four zones modeling of the downdraft biomass gasification process: effects of moisture content and air to fuel ratio, Energy Proc. 52 (2014) 142–149.
[30] C.A. Koufopanosi, G. Maschio, A. Lucchesit, Kinetic modelling of the pyrolysis of biomass and biomass components, Can. J. Chem. Eng. 67 (1989) 75–84. Feb.
[31] T.H. Jayah, L. Aye, R.J. Fuller, D.F. Stewart, Computer simulation of a downdraft wood gasifier for tea drying, Biomass Bioenergy 25 (2003) 459–469.
[32] A. Dufour, E. Masson, P. Girods, Y. Rogaume, A. Zoulalian, Synthesis gas production by biomass pyrolysis: effect of reactor temperature on product distribution, Int. J. Hydrogen Energy 43 (2009) 1726–1734.
[33] J. Xie, W. Zhong, B. Jin, Y. Shao, H. Liu, Simulation on gasification of forestry residues in fluidized beds by Eulerian Lagrangian approach, Bioresour. Technol. 121 (2012) 36–46.
[34] B.L. Gomez-Barea, Modeling of biomass gasification in fluidized bed, Prog. Energy Combust. Sci. 36 (2010) 444–509.
[35] J. Tomeczek, Z. Jastrzçab, B. Gradoń, Lateral diffusion of solids in a fluidized bed with submerged vertical tubes, Powder Technol. 72 (1) (1992) 17–22.
[36] P. Nakod, Modeling and validation of oxy-fired and air-fired entrained flow gasifiers, Int. J. Chem. Phys. Sci. 2 (6) (2013) 2074–2091.
[37] D. Fuentes-Cano, A. Gómez-Barea, S. Nilsson, P. Ollero, Kinetic modeling of tar and light hydrocarbons during the thermal conversion of biomass, Energy Fuel. 30 (2016) 377–385.
[38] F. Marias, A. Fourcault, U. Michon, Modelling of thermal removal of tarsinahightemperature stage fedbyaplasmatorch, Biomass Bioenergy 34 (2010) 1363–1374.
[39] P. Morf, P. Hasler, T. Nussbaumer, Mechanisms and kinetics of homogeneous secondary reactions of tar from continuous pyrolysis of wood chips, Fuel 81 (2002) 843–853.
[40] T.H. Jayah, L. Aye, R.J. Fuller, D.F. Stewart, Computer simulation of a downdraft wood gasifier for tea drying, Biomass Bioenergy 25 (2003) 459–469.
[41] P.P. Dutta, V. Pandey, A.R. Das, S. Sen, D.C. Baruah, Down draft gasification modelling and experimentation of some indigenous biomass for thermal applications, Energy Proc. 54 (2014) 21–34.
[42] A. Al-Akaishi, A. Valera-Medina, C.T. Chong, R. Marsh, CFD analysis of the fluidised bed hydrodynamic behaviour inside an isothermal gasifier with different perforated plate distributors, Energy Proc. 142 (2017) 835–840.
[43] S.P. Shi, S.E. Zitney, M. Shahnam, M. Syamlal, W.A. Rogers, Modelling coal gasification with CFD and discrete phase method, J. Energy Inst. 79 (4) (2016) 217–221.
[44] I. Janajreh, M. Al Shrah, Numerical and Experimental Investigation of Downdraft Gasification of Wood Chips, 65, Energy Conversion and Management, 2013, pp. 783–792.
[45] P. Prasertcharoensuk, D.A. Hernandez, S.J. Bulla, Ana A.N. Phan, Optimisation of a throat downdraft gasifier for hydrogen production, Biomass Bioenergy 116 (2018) 216–226.
[46] A. Slezak, J.M. Kuhlman, L.J. Shadle, J. Spenik, S. Shi, CFD simulation of entrained-flow coal gasification: coal particle density/sizefraction effects, Powder Technol. 203 (1) (2010) 98–108.
[47] C.M. Kinoshita, Y. Wang, Kinetic model of biomass gasification, Sol. Energy 51 (1) (1993) 19–25.
[48] P. Basu, Biomass Gasification and Pyrolysis: Practical Design and Theory, Academic press, Burlington, 2010.
[49] U. Kreibig, M. Quinten, OPTICAL MATERIALS | heterogeneous materials, in: R. D. Guenther (Ed.), Encyclopedia of Modern Optics, Elsevier, Oxford, UK, 2005, ISBN 978-0-12-369395-2.
[50] D. Wang, A. Violi, D.H. Kim, formation of naphthalene, indene, and benzene from cyclopentadiene pyrolysis: a dft, J. Phys. Chem. 110 (14) (2006) 4719–4725.
[51] A.V. Friderichsen, et al., The pyrolysis of anisole (C6H5OCH3) using a hyperthermal nozzle, Fuel 8 (12) (2001) 1747–1755.
[52] E. Savuto, A. Di Carlo, E. Bocci, A. D'Orazio, Development of a CFD model for the simulation of tar and methane steam reforming through a ceramic catalytic filter, Int. J. Hydrogen Energy 40 (25) (2015) 7991–8004.
[53] T.A. Milne, R.J. Evans, N. Abatzoglou, Biomass Gasifier "Tars": Their Nature, Formation, and Conversion, NREL TP-570-25357, Golden, Colorado, Colorado, USA, 1998.